ACS Photonics

Article

pubs.acs.org/journal/apchd5

Self-Assembled Nanoparticle Dimer Antennas for Plasmonic-Enhanced Single-Molecule Fluorescence Detection at Micromolar Concentrations

Deep Punj, Raju Regmi, Alexis Devilez, Robin Plauchu, Satish Babu Moparthi, Brian Stout, Nicolas Bonod, Hervé Rigneault, and Jérôme Wenger*

CNRS, Aix-Marseille Université, Centrale Marseille, Institut Fresnel, UMR 7249, 13013 Marseille, France

Supporting Information

ABSTRACT: Plasmonic antennas offer extremely promising strategies to enhance single molecule fluorescence sensing and breach the limitations set by diffraction. However, the technical difficulty and limited availability of top-down nanofabrication techniques enabling nanometer gap sizes are limiting the impact of plasmonic antennas for biochemical and biophysical applications. Here we demonstrate the effectiveness of self-assembled nanoparticle gap antennas to enhance single molecule fluorescence detection at high concentrations. For a dimer of 80 nm gold nanoparticles with 6 nm gap, we isolate detection volumes down to 70 zL (equivalent to $\lambda^3/3600$) and achieve 600-fold fluorescence enhancement, microsecond transit time, and operation of fluorescence correlation spectroscopy at concentrations exceeding 10 μM. We quantify the near-field detection volume and the fluorescence enhancement for different self-assembled nanoantenna designs using fluorescence correlation spectroscopy. The combination of the fabrication simplicity with the large fluorescence enhancement makes the self-assembled colloidal nanoparticle gap antennas optimal to extend a wide variety of single-molecule applications toward the biologically relevant micromolar concentration regime.

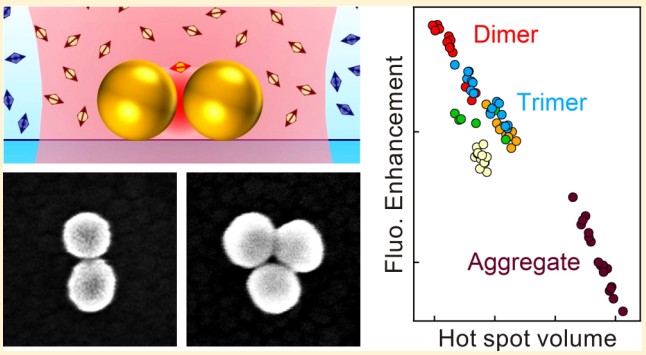

KEYWORDS: *plasmonics, nanoantenna, fluorescence enhancement, fluorescence correlation spectroscopy, gold nanoparticle, self-assembly*

Single molecule microscopy techniques offer a powerful new vision to explore the functioning of elementary components in life sciences and chemistry.[1−3] However, conventional optical approaches are limited by diffraction to observation volumes in the femtoliter (μm^3) range,[4] which forces the use of diluted samples at pico or nanomolar concentrations in order to isolate a single molecule within the observation volume. This low concentration condition is highly restrictive: the majority of enzymatic reactions require concentrations in the micro to millimolar range and, thus, cannot be investigated with single molecule resolution using conventional microscopy techniques.[5−7]

To overcome the concentration limit, light must be confined toward the nanometer scale, far below the classical wavelength size set by the diffraction limit. This challenge is efficiently addressed using nanophotonics and plasmonics.[8−10] Zero-mode waveguides offer a practical solution to confine light at the bottom of subwavelength apertures milled in metal films, reaching attoliter detection volumes.[11−15] To further reduce the detection volume and simultaneously enhance the fluorescence emission, resonant optical nanoantennas open up a large scope of possibilities.[16−21] Remarkable results were obtained recently using antennas fabricated by electron or ion lithography,[22,23] reaching over 1000× enhancement of the fluorescence brightness per molecule in the 10 nm gap region of the antenna. However, classical top-down nanofabrication techniques remain challenging and expensive to operate, especially when predefined and well-controlled gap sizes of a few nanometers are required.[24] This difficulty is currently considered to limit the broad use of plasmonic antennas in biochemistry laboratories.[5]

Bottom-up wet-chemistry approaches offer a powerful alternative to fabricate the nanoantennas as they combine specific advantages: simple implementation, low operation cost, realization of gap sizes below 10 nm, and use of single crystalline structures.[25,26] The self-assembly of colloidal gold nanoparticles templated by DNA double strands[27−30] or DNA origami[31−34] has thus attracted much interest to realize dimer gap antennas. To further simplify the nanofabrication and avoid the use of DNA structures, drying of colloidal nanoparticle suspension provides straightforward access to resonant optical

Received: March 26, 2015
Published: July 9, 2015

DOI: 10.1021/acsphotonics.5b00152
ACS Photonics 2015, 2, 1099−1107

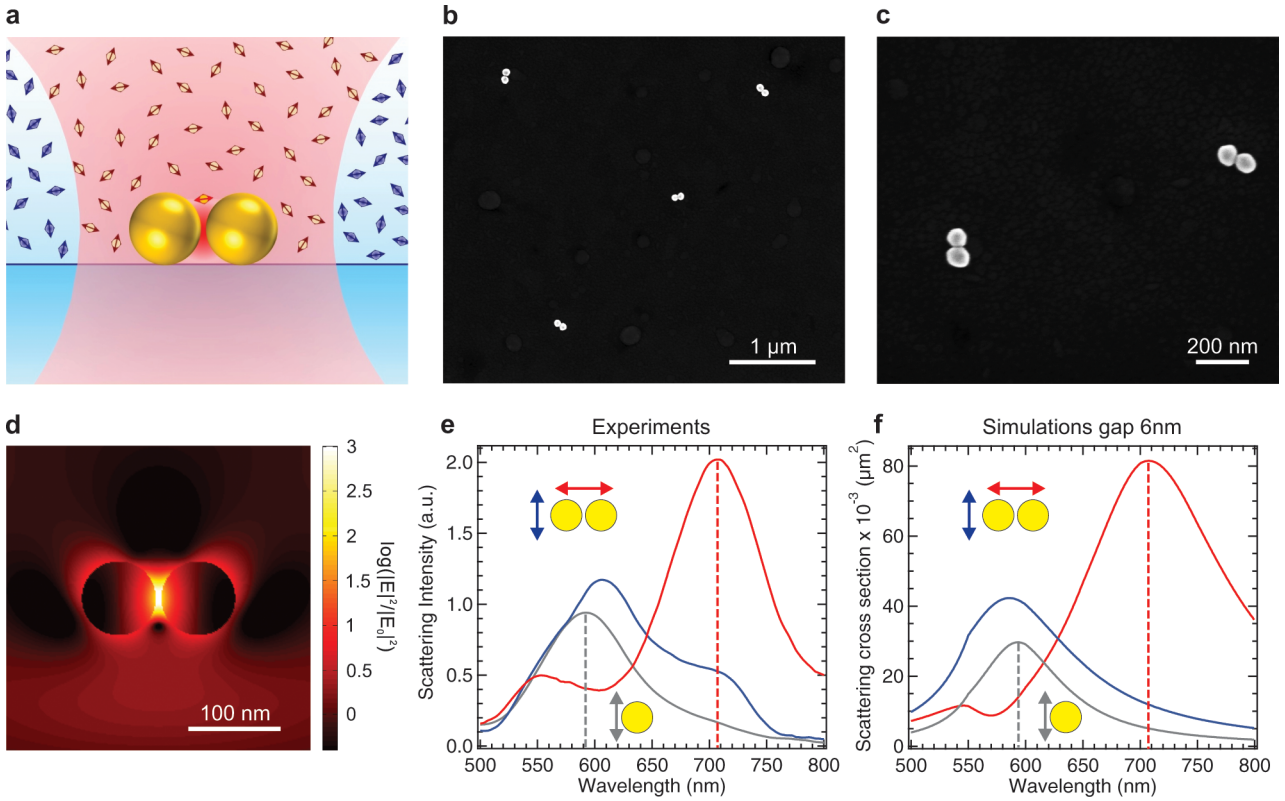

Figure 1. Gold nanoparticle dimer antenna for single molecule analysis at high concentrations. (a) Schematic of a dimer antenna illuminated by a diffraction-limited focused laser beam. A solution of fluorescent molecules at micromolar concentration covers the antenna, only a few molecules randomly diffuse in the hot spot inside the nanoparticles gap, while thousands of molecules are in the diffraction-limited confocal volume. (b, c) Scanning electron microscopy (SEM) images of nanoparticle dimers self-assembled by colloidal drying. Throughout this study, the gold nanoparticle diameter is 80 nm. (d) Excitation intensity enhancement (log scale) for a nanoparticle dimer with 6 nm gap computed using Mie theory. The incoming light has a wavelength of 633 nm and is polarized parallel to the dimer axis. (e, f) Dark-field scattering spectra on a nanoparticle dimer (red and blue traces, parallel and perpendicular polarizations) and on a monomer (gray traces). The dimer longitudinal mode at 705 nm is clearly red-shifted as compared to the transverse mode at 590 nm. The spectra in (e) are experimental data, the ones in (f) are simulated with the surrounding medium effective index n_{eff} = 1.5, determined from the scattering spectra of a monomer and a gap size of 6 nm set so as to match the longitudinal dimer resonance (see Supporting Information, Figures S2 and S3).

antennas with gap sizes down to a few nanometers.[35−40] Such gap antennas appear highly promising to enhance the analysis of single fluorescent molecules at high concentrations, and go beyond the results obtained with single spherical gold nanoparticles[41−45] or rod-shaped nanoparticles.[46−48] However, this specific application imposes another major challenge, that is to retrieve the useful information stemming from the nanoantenna gap region (hot spot) from the background created by the other fluorescent molecules in the confocal detection volume.[23] At high micromolar concentrations, this fluorescence background can outshine the signal originating from the hot spot and thus severely limit the applicability of plasmonic antennas for solution-based measurements.[49] Moreover, the binding of molecules to the metal surface can generate artifactual fluorescence fluctuations and significantly complicate the analysis.[41,50]

Here we use self-assembled gold nanoparticle dimers with 6 nm gap to analyze single molecule fluorescence in solutions of 13 μM concentration using fluorescence correlation spectroscopy (Figure 1a). Drying of droplets containing the colloidal suspension of gold nanoparticles provides a simple and direct approach to self-assemble plasmonic antennas with nanometer gap sizes (Figure 1b,c). Remarkably, this simplicity does not come at the expense of performance, as we demonstrate gap-antenna detection volumes of 70 zeptoliter, fluorescence enhancement up to 600-fold, microsecond transit time and fluorescence correlation spectroscopy at concentrations exceeding 10 μM. Another major result of this study is that we quantify the near-field detection volume and the fluorescence enhancement for different self-assembled nanoantenna designs involving dimers, trimers, and higher numbers of nanoparticles. Such quantitative analysis has never been reported so far. Altogether, the ease of nanofabrication and the large fluorescence enhancement make the self-assembled colloidal nanoparticle antennas optimal for single molecule sensing at the biologically relevant micromolar concentration regime. This work shall expand the applicability of plasmonic antennas for solution-based measurements.

Drying of colloidal suspensions of 80 nm gold nanoparticles at concentrations of 10^9 particles/mL naturally self-assemble the nanoparticles into nanoantenna structures from which dimer antennas can be selected (see Methods). Typical dimer antennas are shown on Figures 1b,c and 2a. An overview of the sample is displayed in Supporting Information, Figure S1. Throughout this work, we use localization marks to identify the relevant nanoantennas with scanning electron microscopy (SEM) and correlate the SEM images with the experiments performed on the confocal optical microscope. The SEM imaging is used to support our claim of single nanoantenna in the focus and explore a wide variety of assembly configurations.

DOI: 10.1021/acsphotonics.5b00152
ACS Photonics 2015, 2, 1099−1107

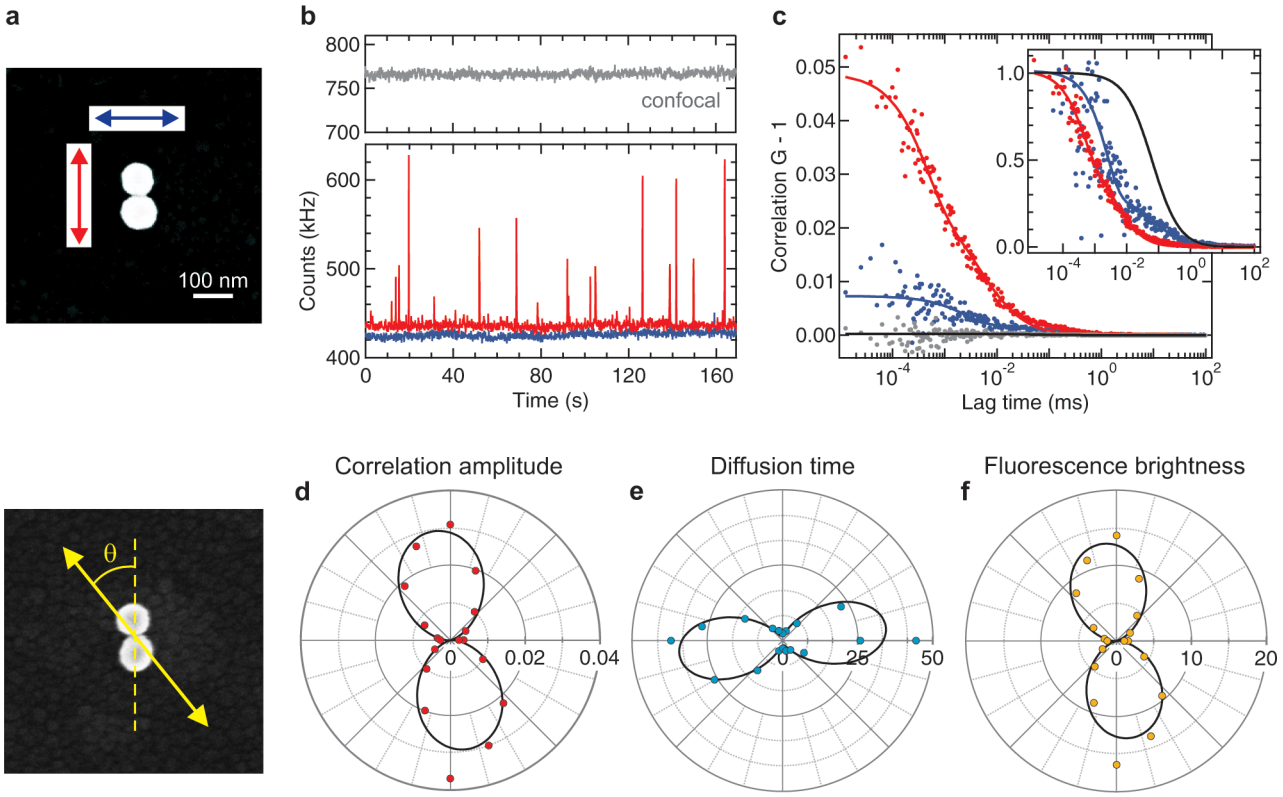

Figure 2. Enhanced fluorescence analysis with a nanoparticle dimer: (a) SEM image of the dimer; (b) Fluorescence time trace; and (c) FCS correlation function (dots, raw data; lines, numerical fits). Red traces correspond to a laser polarization parallel to the dimer axis, and blue traces are for perpendicular orientation. The reference data taken without dimer antenna (confocal configuration) are also displayed in gray for a direct comparison. All experiments are performed with 13.3 μM concentration of Alexa Fluor 647 and 200 mM of methyl viologen as chemical quencher. The excitation power at 633 nm is 10 μW. The inset in (c) shows the amplitude-normalized correlation functions to better show the faster temporal dynamics with the antenna, the black curve is the confocal reference. Numerical results from the FCS data analysis are summarized in Table S1 of the Supporting Information. (d–f) Dipolar response of the experimental results on a dimer antenna while turning the laser polarization orientation. The raw FCS data are shown in Supporting Information, Figure S7. The polar graphs represent the raw correlation amplitude (d), the diffusion time extracted from FCS fits (e), and the molecular fluorescence brightness (f) as a function of the laser polarization orientation θ. Dots are experimental data, lines are numerical fits using a $\cos^2$ function for (d and f) and a $\sin^4$ function for (e).

However, SEM is not a mandatory step for the experiments: dimer antennas can be easily identified in confocal microscopy thanks to their distinctive extinction and polarization-dependent response. So the experiments described here can be easily reproduced in every biochemical laboratory without the need for electron microscopy prior to the optical experiments.

Polarization-resolved dark field spectroscopy is used to characterize the plasmonic properties of the nanoantennas and measure the gap size, providing a more accurate characterization than direct SEM image analysis. Representative spectra for the dimer and monomer antennas are shown in Figure 1e. While the monomer response bears a single peak at 590 nm independent of the polarization orientation, the dimer shows a characteristic dipolar polarization dependence, with a significant red-shift of the plasmon peak up to 705 nm when the polarization is aligned with the longitudinal dimer axis. The experimental spectra are compared to numerical simulations performed using the generalized Mie theory[54] to further validate the experimental procedure and quantify the gap size between the nanoparticles (Figure 1d,f). For the simulations, the effective refractive index surrounding the nanoparticles was determined to n_{eff} = 1.5 so as to best fit the measured spectra of the monomer (Supporting Information, Figure S2). This is a standard procedure also used in refs29 and 32. The n_{eff} = 1.5 parameter value was then fixed for the simulations on the dimers, the only free parameter being the gap size, which was tuned so as to best fit the longitudinal mode in the experimental spectra. A gap size of 6 ± 2 nm provides an excellent agreement with the experimental data, for both the longitudinal and transverse modes (Figure 1e,f). The 2 nm uncertainty is related to the statistical distribution of nanoparticles sizes and shapes, as shown by SEM images. More details about the dependence of the local surface plasmon resonance wavelength on the refractive index and gap size are given in the Supporting Information, Figure S3. We also checked that the red-shift of the dimer plasmon resonance decreases when an additional PEG layer is used to enlarge the gap size between nanoparticles (Supporting Information, Figure S4). Altogether, the dark field spectra indicate strong plasmonic coupling in our dimer structure, revealing nanometer gap size. Supplementary computations of the absorption, scattering, and extinction cross sections are displayed in Supporting Information, Figure S5.

The large intensity enhancement in the nanometer gap enables single molecule detection at high micromolar concentrations. A major difficulty set by the experiment scheme depicted in Figure 1a is that the enhanced fluorescence signal stemming from the dimer hot spot is hidden by the large fluorescence background from several thousands of freely diffusing molecules within the diffraction-limited confocal

DOI: 10.1021/acsphotonics.5b00152
ACS Photonics 2015, 2, 1099–1107

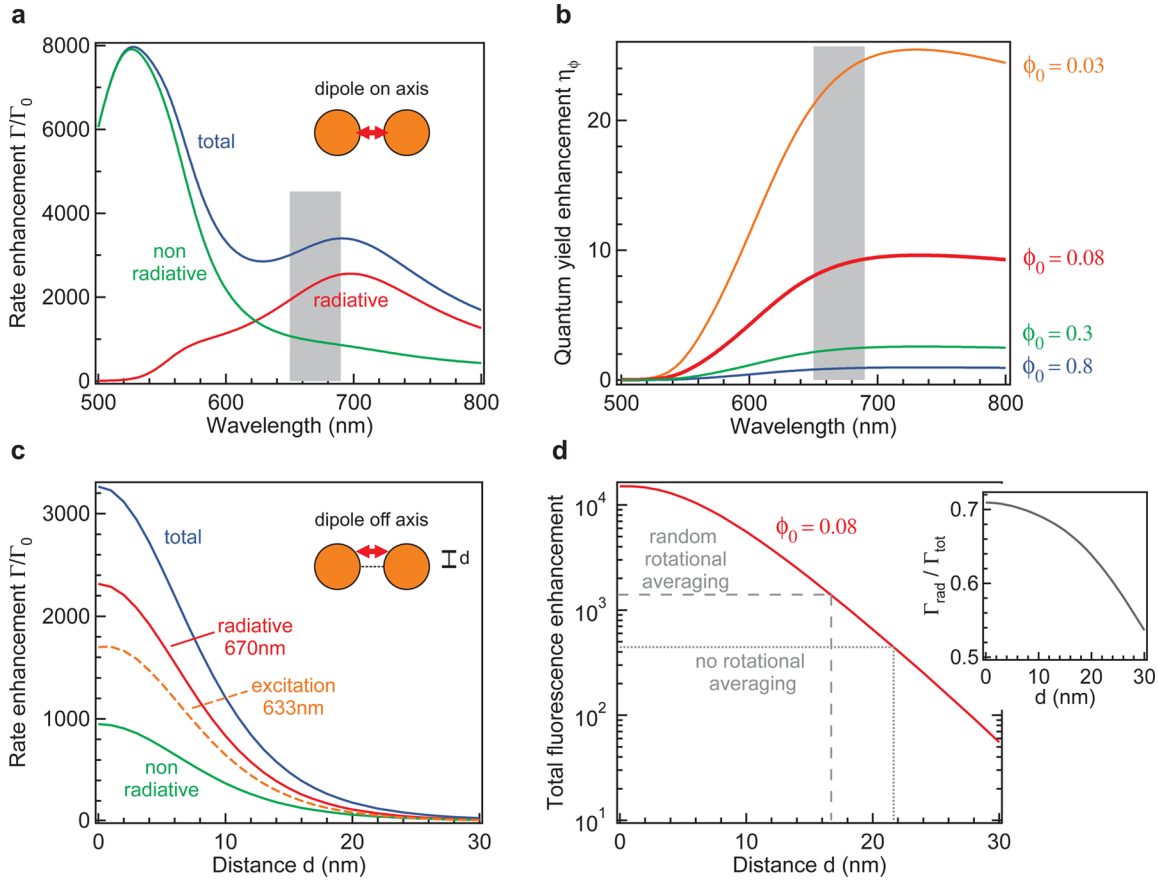

Figure 3. Photokinetics enhancement in a gold dimer nanoantenna with 80 nm diameter and 6 nm gap. (a) Decay rate enhancement as a function of the emission wavelength for a perfect dipole emitter with parallel orientation located in the dimer center. The gray shaded area indicates the 650−690 nm range used for fluorescence detection in the experiments. (b) Quantum yield enhancement deduced from (a) for different values of the reference quantum yield ϕ_0 in solution. The case $\phi_0 = 0.08$ (thick red line) corresponds to the experiments. (c) Decay rate enhancement for a dipole emitter with parallel orientation as a function of the distance d from the dimer axis. The dipole emits at 670 nm while the excitation is at 633 nm. (d) Net fluorescence enhancement as a function of the distance d to the dimer axis, computed from (c) for a dye with a reference quantum yield of 8%. The lines indicate the typical distances d corresponding to the experimental fluorescence enhancement, depending on whether random orientational averaging is taken into account or not. The inset displays the ratio of radiative to total decay rate for a perfect dipole emitter.

volume. To extract the useful information from the nanoantenna, we take advantage of the higher fluorescence enhancement factors obtained with emitters of low quantum yield.[23,45] Here, we use Alexa Fluor 647 dyes and add 200 mM of methyl viologen to quench the dye quantum yield from 30% to 8%.[23] Without the chemical quencher, the fluorescence background contribution at 10 μM concentration is too high for the avalanche photodetectors, and no useful signal contribution from the antenna hot spot could be detected.

We analyze the fluorescence signal F by fluorescence correlation spectroscopy (FCS) to quantify the hot spot detection volume and fluorescence enhancement.[2,4,23] FCS computes the temporal correlation of the fluorescence signal $G(\tau) = \langle F(t)\cdot F(t+\tau)\rangle/\langle F(t)\rangle^2$, where τ is the delay (lag) time and $\langle\ \rangle$ indicates time averaging. An essential feature of FCS is that the molecules contribute to G in proportion to the square of their fluorescence brightness.[2] Hence, a large fluorescence enhancement in the hot spot improves the signal-to-background contrast in FCS by a quadratic manner.[23,49] The Methods section briefly presents the most relevant information about the FCS analysis. Full details about the procedure and equations for FCS analysis are given in the Supporting Information, Section 6, and an additional validation is reported in Supporting Information, Section 11. We also stress that the molecules constantly diffuse in a Brownian fashion around the nanoantenna; thus, the observations are virtually free of photobleaching.

The FCS analysis extracts the hot spot contribution and quantifies the fluorescence enhancement, which clearly depends on the polarization orientation respective to the dimer axis. Figure 2 shows the fluorescence time trace and FCS correlation function for two orthogonal polarizations. All experiments were taken at a concentration of 13.3 μM of Alexa Fluor 647, corresponding to about 4000 molecules in the 0.5 fL confocal detection volume. In the absence of the nanoantenna, the correlation amplitude is barely detectable at 1/4000 = 2.5 × 10^{-4}. In contrast, the fluorescence time traces for nanoantennas show larger relative fluctuations and remarkably higher correlation amplitudes, which are maximized when the polarization is aligned with the dimer axis. These FCS features can only be obtained by monitoring a small number of molecules with high apparent brightness. In the case of excitation polarization parallel to the dimer axis (Figure 2c, red traces), FCS analysis quantifies an average number of N^* = 0.55 molecules (see Supporting Information, Table S1). Given the calibrated Alexa concentration of 13.3 μM, this number of molecules corresponds to a detection volume in the nanoantenna hot spot of 69 zL (1 zL = 10^{-21}L) or equivalently to a

DOI: 10.1021/acsphotonics.5b00152
ACS Photonics 2015, 2, 1099−1107

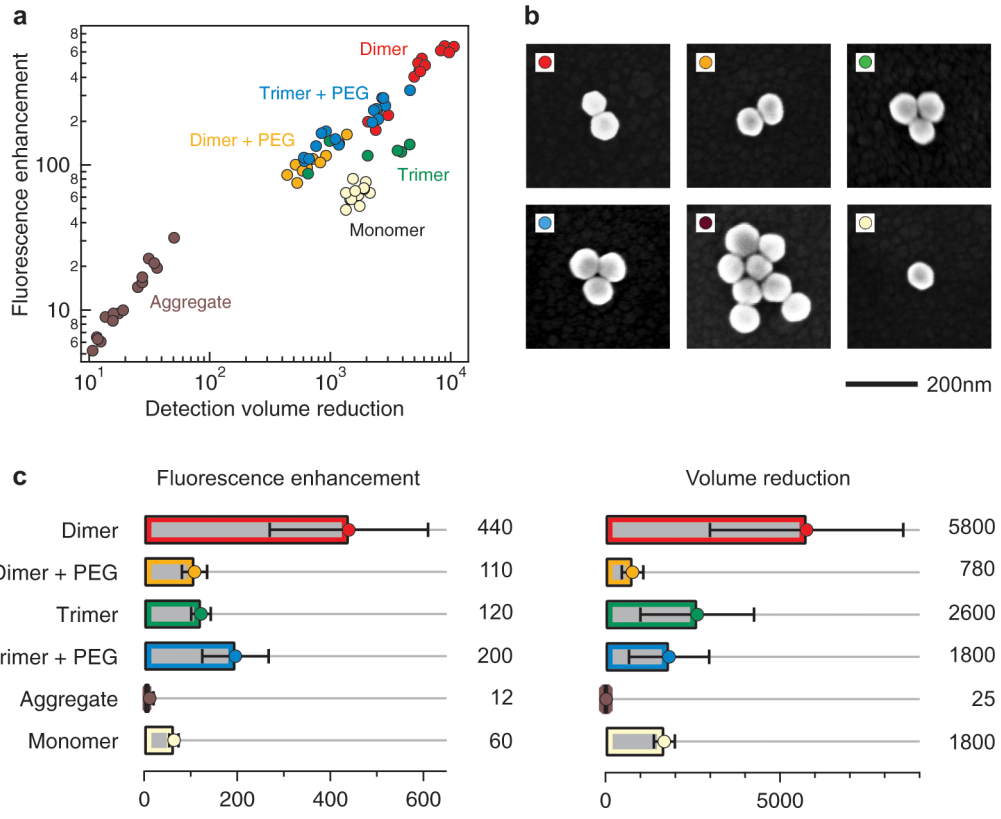

Figure 4. Fluorescence enhancement and volume reduction for self-assembled nanoparticle antennas. (a) Scatter plot of fluorescence enhancement versus volume reduction as compared to the diffraction-limited confocal reference. The markers represent different antennas tested. Their color is associated with different configurations and to the presence of an additional PEG layer around the nanoparticles, as shown by SEM images of typical structures in (b). (c) Average fluorescence enhancement and volume reduction for the different antenna configurations. Error bars indicate the standard deviation, numerical values at the right of the graphs indicate the average value over the different samples.

detection volume reduction of $N_{sol}/N^* = 7300\times$ as compared to the diffraction-limited confocal volume. Remarkably, the volume deduced from FCS corresponds well to the $60 \times 60 \times 15$ nm^3 = 54 zL value expected from the numerical simulations (Figure 1d), considering a lateral YZ extension of 60 nm and a mean axial distance of 15 nm. A more elaborate computation considering the toroidal shape of the detection volume with typical radius 15 nm concludes to 67 zL, which comes even closer to the experimental value.

As an additional feature illustrating the near-field origin of the FCS signal, the diffusion time is clearly reduced down to $\tau^* = 1.9$ μs with the nanoantenna, well below the $\tau_{conf} = 64$ μs characteristic diffusion time for a diffraction-limited spot (Figure 2c, inset). Considering the equivalent average size of 25 nm to yield a detection volume of 69 zL and given the 280 nm beam waist at focus, the diffusion time in the hot spot is estimated to $\tau^* = 4\tau_{conf}(25/280)^2 = 2$ μs following the model in ref 41. This value stands in excellent agreement with the experimental observation and further confirms the reasonable estimates derived from the FCS analysis. Moreover, this clear diffusion time reduction indicates that molecular adhesion artifacts are absent in our experiments.

The dipolar nature of the polarization response on a dimer nanoantenna is emphasized in Figure 2d–f (raw FCS correlograms are shown in Supporting Information, Figure S7, for various polarization angles). Both the correlation amplitude $G(0)$ (Figure 2d) and the fluorescence brightness per molecule (Figure 2f) follow a $\cos^2$ law, with a clear maximum when the polarization is set along the dimer axis. Interestingly, we also observe a polarization dependence of the diffusion time across the hot spot detection volume (Figure 2e, this data corresponds also to the width of the FCS correlogram). For this observable, a minimum is found when the polarization is aligned with the dimer axis, corresponding to a maximum in the confinement of light inside the nanoantenna gap.

Simultaneously, the FCS analysis quantifies the fluorescence brightness per molecule in the gap region to $Q^* = 109$ kHz, which corresponds to a fluorescence enhancement of $Q^*/Q_{sol} = 575 \pm 40$ times. The fluorescence bursts seen in Figure 2a time trace allow to independently estimate the fluorescence enhancement factor. The bursts are only present if the laser polarization is aligned with the dimer axis, and occur when single molecules cross the antenna hot spot. Following the approach in refs 46 and 47, the fluorescence enhancement deduced from the maximum burst intensity amounts to 195/0.19 = 1030-fold. This supports well our claim of enhanced fluorescence, and is even higher than the 575-fold claim deduced from FCS as a consequence of the preferential selection by burst analysis of the best events corresponding to the dye located in the hot spot center with parallel orientation.

The fluorescence enhancement results from different phenomena: higher local excitation intensity leading to increased excitation rate, increased radiative emission rate for the dipole emitter inside the gap, and new energy decay routes opened by nonradiative energy transfer to the metal. Numerical simulations using Mie theory assess the relative role of these phenomena by computing the radiative Γ_{rad}, nonradiative Γ_{nr}

DOI: 10.1021/acsphotonics.5b00152
ACS Photonics 2015, 2, 1099–1107

and total decay rates Γ_{tot}, following the approach detailed in refs 29 and 54. Figure 3a shows the spectral dependence for a perfect dipole emitter with parallel orientation located in the antenna center. Other orientations yield comparatively negligible rate enhancements. Again, a resonance is present around 700 nm, which corresponds nicely with the resonance in the scattering spectra seen in Figure 1e,f. For this resonance, the emitters decay essentially radiatively as the nonradiative losses remain moderate. The second resonance around 520 nm is essentially nonradiative and involves quadrupolar modes along with high intrinsic losses of gold in this spectral window.

We then compute the quantum yield enhancement from the decay rates in Figure 3a. This enhancement depends on the reference quantum yield ϕ_0 for the dye in open solution (without antenna). Following the approach in ref 51, the quantum yield enhancement is given by the following formula:

$$\eta_\phi = \frac{\Gamma^*_{rad}/\Gamma_0}{\phi_0\Gamma^*_{tot}/\Gamma_0 + (1-\phi_0)} \quad (1)$$

where Γ^*_{rad}/Γ_0 and Γ^*_{tot}/Γ_0 are the radiative and total decay rate enhancement computed in Figure 3a. Figure 3b shows the spectral evolution for a selection of reference quantum yields. In agreement with previously reported works,[52,53] we find that the quantum yield bears a more pronounced enhancement for wavelengths red-shifted as compared to the LSPR. This is a consequence of the fact that the peak wavelength for enhanced nonradiative decay rate coincides with the LSPR wavelength but then drops rapidly toward the red side of the LSPR, while the radiative rate has a longer tail toward the red. As expected, we also observe a higher quantum yield enhancement when the reference ϕ_0 is lower, leaving more space for plasmonic improvement.

While the case with the dipole emitter in the dimer center provides the best enhancement values, it does not reflect fairly the experimental findings as the FCS data is spatially averaged over all dipole locations and orientations in the gap area. Therefore, we investigate the lateral position dependence for a dipole emitter with parallel orientation shifted by a distance d from the dimer center and compute the different rates corresponding to radiative, nonradiative, total, and excitation transitions (Figure 3c). All rates evolve with the distance following an approximative Gaussian shape with a typical 15 nm distance at $1/e^2$. These rates allow to compute the net fluorescence enhancement as the product of the quantum yield enhancement times the local excitation intensity enhancement (Figure 3d). The average 440× fluorescence enhancement found with the dimer antennas corresponds to a distance of d = 22 nm if we neglect rotational diffusion and consider only dipoles with parallel orientation. Instead, if random rotational averaging is taken into account, the enhancement projected on the X axis must be approximately 3× higher and corresponds to a distance of d = 16 nm, as seen on Figure 3d. Both estimates point around 20 nm, in good agreement with the other experimental observables deduced from FCS (detection volume, diffusion time). Lastly, the influence of quenching remains moderate as the apparent quantum yield stays in the range 55−70% for all distances to the dimer axis (Figure 3d, inset).

We have applied the same characterization procedure to a wide range of self-assembled antenna designs, including monomers, dimers, trimers and aggregates of more than five nanoparticles. We have also considered the additional use of a poly ethylene glycol (PEG) layer of 6 nm thickness surrounding the gold nanoparticles to enlarge the gap size. Our main results are summarized in Figure 4, as we focus on the fluorescence brightness enhancement per molecule Q^*/Q_{sol} and the detection volume reduction N_{sol}/N^*. Remarkably, the dimer antenna with minimum gap size stand out as the best configuration leading to the maximum fluorescence enhancement and volume reduction. The additional PEG layer enlarges the dimer gap to about 13 nm (Supporting Information, Figure S4), which leads to a significantly lower fluorescence enhancement and larger detection volume. The trimers show a lower performance as compared to the dimers without PEG, but their response is almost insensitive to the polarization orientation (raw data are shown in Supporting Information, Figure S8). Looking at the influence of the additional PEG layer in the case of trimers, we find a higher fluorescence enhancement in the presence of PEG. We relate this effect to the better overlap of the trimers plasmonic response with the excitation wavelength in the presence of PEG, leading to a slightly higher excitation enhancement as compared to trimers without PEG (see Supporting Information, Figures S8b and S9). Considering the case of random aggregates, only very poor performances could be obtained, emphasizing the interest for dimer nanoantennas.

In summary, we demonstrate the effectiveness of self-assembled nanoparticle antennas to enhance single molecule fluorescence detection at high micromolar concentrations. In the best configuration of a dimer with 6 nm gap, we isolate detection volumes down to 70 zL, accompanied by a 600-fold fluorescence enhancement and microsecond transit time. This performance is comparable to the results obtained with an "antenna-in-box" fabricated by state-of-the-art focused ion beam[23] but with a much simpler and more affordable bottom-up approach, which can be envisioned even without the use of SEM. The combination of self-assembled nanoantennas with fluorescence correlation spectroscopy significantly expands the applicability of plasmonic antennas for a wide variety of biosensing and single-molecule applications at the biologically relevant micromolar concentration regime.

METHODS

Nanoantenna Fabrication. Throughout this work, we use commercial gold nanoparticles (BBI Solutions) of 80 nm diameter covered with citrate surfactant. The size dispersion was studied by TEM in the Supporting Information of ref 31 and was found below 10%. The nanoparticles are rinsed and diluted in pure water to reach concentrations of typically 10^9 particles/mL, then they are dispersed and dried on an ITO-coated glass coverslip. Upon drying, the colloidal nanoparticles self-assemble into dimers or higher order structures, as shown on the typical SEM image in Figure S1 of the Supporting Information. The positions of relevant antenna structures are identified by SEM thanks to markings on the ITO coated coverslip. These positions and markings are then used to locate the same set of antennas while performing experiments on the confocal microscope. However, we stress that these markings and the SEM imaging are not necessary steps: dimer antennas can be easily identified thanks to their distinctive polarization-dependent response and their dark-field scattering spectra (Figures 1e and 2d−f).

In order to tune the gap size in the case of dimers and trimers, we use a classic approach of thiol binding to adhere a sulfhydryl-capped PEG chain onto the gold surface. We use

DOI: 10.1021/acsphotonics.5b00152
ACS Photonics 2015, 2, 1099−1107

poly(ethylene glycol) methyl ether thiol (mPEG-SH) with molecular weight 800 Da which has a spacer arm of 6.3 nm. Gold nanoparticles are cleaned with anhydrous ethanol, then incubated for overnight at room temperature in 1 mM mPEG-SH (Sigma-Aldrich) in anhydrous ethanol (Sigma) and then washed thoroughly with ethanol, Milli-Q ultrapure water, and isopropyl alcohol and finally dispersed and dried on ITO-coated coverslip. Prior to FCS experiments, the PEG layer is removed by 10 min UV/ozone cleaning (PSD-UV cleanr, Novascan) followed by gentle rinsing with a 1:1 water−ethanol mixture and nitrogen drying.

Experimental Setup. The experimental setup is based on a confocal inverted microscope with a Zeiss C-Apochromat 40× 1.2 NA water-immersion objective. For dark-field spectroscopy, the illumination is provided by a 100 W halogen lamp to form a collimated linearly polarized beam incoming at normal incidence on the antenna. A beam block is inserted close to the microscope objective back focal plane to stop the illumination and collect only the scattered light from the antenna. The detection is performed in confocal mode (50 μm pinhole conjugated to the object plane) with a Horiba iHR320 spectrograph equipped with a Peltier-cooled CCD detector. For FCS measurements, the excitation source is a linearly polarized He−Ne laser operating at 633 nm. A dichroic mirror (Omega Filters 650DRLP) and a long pass filter (Omega Filters 640AELP) separate the fluorescence light from the epi-reflected laser and elastically scattered light. A 30 μm confocal pinhole defines a detection volume calibrated to 0.5 fL. After the confocal pinhole, the detection is performed by two avalanche photodiodes (Micro Photon Devices by PicoQuant MPD-5CTC) with 670 ± 20 nm fluorescence bandpass filters. The fluorescence intensity temporal fluctuations are analyzed with a hardware correlator (Flex02−12D/C correlator.com, Bridgewater, NJ, with 12.5 ns minimum channel width). Each individual FCS measurement is obtained by averaging 20 runs of 5 s duration.

Scanning electron microscopy images are performed on a FEI DB235 microscope with field emission gun and 5 kV acceleration voltage, providing about 4−5 nm spatial resolution.

Fluorescence Correlation Spectroscopy Analysis. The analysis of the FCS data considers a model with two fluorescent species of different numbers of molecules and fluorescence brightness: N^* molecules in the dimer hot spot volume with brightness Q^*, and N_0 background molecules with brightness Q_0 away from the hot spot. We are primarily interested in quantifying the hotspot fluorescence brightness Q^* and detection volume which amounts to the number of molecules N^* for a calibrated sample concentration. This quantification requires only the value of the correlation function at zero lag time:

$$G(0) = 1 + \frac{N_0 Q_0^{\,2} + N^* Q^{*2}(1 + n_T^*)}{(N_0 Q_0 + N^* Q^*)^2} \tag{2}$$

Here n_T^* represents the dark state blinking amplitude for the molecules in the hotspot. Equation 1 shows that the different fluorescent species contribute in proportion to the square of their relative fluorescence brightness, enabling the extraction of a significant FCS signal from the hot spot under conditions of large background. Using the known value of the average total fluorescence intensity F and after some algebra (detailed in the Supporting Information, Section 6), we get the expressions needed to quantify the hot spot influence:

$$Q^* = \frac{F^2(G(0) - 1) - N_0 Q_0^{\,2}}{(F - N_0 Q_0)(1 + n_T^*)} \tag{3}$$

$$N^* = \frac{(F - N_0 Q_0)^2}{F^2(G(0) - 1) - N_0 Q_0^{\,2}}(1 + n_T^*) \tag{4}$$

The fluorescence brightness Q_0 is set according to the value found for the confocal reference Q_{conf}. For dimers, the number of background molecules N_0 is deduced from the fluorescence intensity when the excitation polarization is set perpendicular to the dimer axis. For trimers and aggregates, N_0 is obtained from the value found at the glass−water interface without nanoantennas, corrected by a factor of $C = 1 - N(d/2w)^2$ to account for the screening induced by the nanoparticles (d is the nanoparticle diameter, w = 280 nm is the laser beam waist at focus, and N is the number of nanoparticles). Typically, C amounts to 0.94 for trimers of 80 nm nanoparticles.

Numerical Simulations. Scattering efficiencies were calculated with an in-house numerical method based on the generalized Mie theory (GMT).[54] Due to intense coupling between nanoparticles in the dimer antenna, the GMT calculations require a high truncation order in the multipole expansion to ensure the convergence. Here we use multipole orders up to N = 30 for each scatterer. From the system total T matrix,[55] we derive analytic expressions for the electromagnetic properties of the antenna, such as decay rates, local fields, and far-field emission.[54] Single fluorescent molecules are modeled as dipolar electric sources by taking the first electric term in the outgoing multipole expansion. The total and radiative decay rate enhancements are then obtained by normalizing the emitted power in the presence of the antenna by the emitted power in the homogeneous background medium, P_0.[53,54] Notably, the total emitted power is evaluated by time averaging $P \equiv -j_{src} \cdot E_{loc}$ over one period, where E_{loc} is the electric field produced by the source current while taking into account interactions with the antenna structure. Some of the power emanating from the dipole emitter will be dissipated in the antenna, while the rest will be radiated off into the far field where it can be detected. The calculation of the radiated power consists of integrating the Poynting vector in the far-field limit derived from the scattered field Mie coefficients. The expressions of the total and radiated powers are analytically derived in the multipolar framework as detailed in ref 54. The refractive index of gold was tabulated according to the ref 56.

■ ASSOCIATED CONTENT

Supporting Information

Wide field scanning electron microscope image, effective refractive index for the surrounding medium, gap size estimates, absorption, scattering and extinction cross sections, PEG spacer influence, correlation traces versus excitation polarization on a nanoparticle dimer, experimental data on trimers of nanoparticles, excitation intensity distribution on a trimer of nanoparticles, fluorescence lifetimes and decay traces on dimer and trimer antennas, simulations of FCS and TCSPC results, luminescence background when no fluorescent dye is present. The Supporting Information is available free of charge on the ACS Publications website at DOI: 10.1021/acsphotonics.5b00152.

DOI: 10.1021/acsphotonics.5b00152
ACS Photonics 2015, 2, 1099−1107

AUTHOR INFORMATION

Corresponding Author

*E-mail: jerome.wenger@fresnel.fr.

Notes

The authors declare no competing financial interest.

ACKNOWLEDGMENTS

The research leading to these results has received funding from the European Commission's Seventh Framework Programme (FP7-ICT-2011-7) under Grant Agreements 288263 (Nano-Vista) and ERC StG 278242 (ExtendFRET), and from the French Agence Nationale de la Recherche under Contract ANR-11-BS10-002-02 TWINS. R.R. is supported by the Erasmus Mundus Doctorate Program Europhotonics (Grant 159224-1-2009-1-FR-ERA MUNDUS-EMJD).

REFERENCES

(1) Craighead, H. G. Future lab-on-a-chip technologies for interrogating individual molecules. *Nature* **2006**, *442*, 387−393.

(2) Zander, C.; Enderlein, J.; Keller, R. A. *Single-Molecule Detection in Solution: Methods and Applications*; VCH-Wiley: Berlin/New York, 2002.

(3) Eggeling, C.; Ringeman, C.; Medda, R.; Schwarzmann, G.; Sandhoff, K.; Polyakova, S.; Belov, V. N.; Hein, B.; von Middendorff, C.; Schönle, A.; Hell, S. W. Direct observation of the nanoscale dynamics of membrane lipids in a living cell. *Nature* **2009**, *457*, 1159−1162.

(4) Haustein, E.; Schwille, P. Single-molecule spectroscopic methods. *Curr. Opin. Struct. Biol.* **2004**, *14*, 531−540.

(5) Holzmeister, P.; Acuna, G. P.; Grohmann, D.; Tinnefeld, P. Breaking the concentration limit of optical single-molecule detection. *Chem. Soc. Rev.* **2014**, *43*, 1014−1028.

(6) Punj, D.; Ghenuche, P.; Moparthi, S. B.; de Torres, J.; Grigoriev, V.; Rigneault, H.; Wenger, J. Plasmonic antennas and zero-mode waveguides to enhance single molecule fluorescence detection and fluorescence correlation spectroscopy toward physiological concentrations. *WIREs Nanomed Nanobiotechnol* **2014**, *6*, 268−282.

(7) Tinnefeld, P. Single molecule detection: Breaking the concentration barrier. *Nat. Nanotechnol.* **2013**, *8*, 480−482.

(8) Novotny, L.; van Hulst, N. Antennas for light. *Nat. Photonics* **2011**, *5*, 83−90.

(9) Schuller, J. A.; Barnard, E. S.; Cai, W. S.; Jun, Y. C.; White, J. S.; Brongersma, M. L. Plasmonics for extreme light concentration and manipulation. *Nat. Mater.* **2010**, *9*, 193−204.

(10) Halas, N. J.; Lal, S.; Chang, W. S.; Link, S.; Nordlander, P. Plasmons in strongly coupled metallic nanostructures. *Chem. Rev.* **2011**, *111*, 3913−3961.

(11) Levene, M. J.; Korlach, J.; Turner, S. W.; Foquet, M.; Craighead, H. G.; Webb, W. W. Zero-mode waveguides for single-molecule analysis at high concentrations. *Science* **2003**, *299*, 682−686.

(12) Uemura, S.; Aitken, C. E.; Korlach, J.; Flusberg, B. A.; Turner, S. W.; Puglisi, J. D. Real-time tRNA transit on single translating ribosomes at codon resolution. *Nature* **2010**, *464*, 1012−1017.

(13) Wenger, J.; Gérard, D.; Aouani, H.; Rigneault, H.; Lowder, B.; Blair, S.; Devaux, E.; Ebbesen, T. W. Nanoaperture-enhanced signal-to-noise ratio in fluorescence correlation spectroscopy. *Anal. Chem.* **2009**, *81*, 834−839.

(14) Lu, G.; Li, W.; Zhang, T.; Yue, S.; Liu, J.; Hou, L.; Li, Z.; Gong, Q. Plasmonic-Enhanced Molecular Fluorescence within Isolated Bowtie Nano-Apertures. *ACS Nano* **2012**, *6*, 1438−1448.

(15) Flauraud, V.; van Zanten, T. S.; Mivelle, M.; Manzo, C.; Garcia-Parajo, M. F.; Brugger, J. Large-Scale Arrays of Bowtie Nanoaperture Antennas for Nanoscale Dynamics in Living Cell Membranes. *Nano Lett.* **2015**, *15*, 4176.

(16) Garcia-Parajo, M. F. Optical antennas focus in on biology. *Nat. Photonics* **2008**, *2*, 201−203.

(17) Mivelle, M.; van Zanten, T. S.; Garcia-Parajo, M. F. Hybrid photonic antennas for subnanometer multicolor localization and nanoimaging of single molecules. *Nano Lett.* **2014**, *14*, 4895−4900.

(18) Acimovic, S. S.; Kreuzer, M. P.; Gonzalez, M. U.; Quidant, R. Plasmon near-field coupling in metal dimers as a step toward single-molecule sensing. *ACS Nano* **2009**, *3*, 1231−1237.

(19) Ureña, E. B.; Kreuzer, M. P.; Itzhakov, S.; Rigneault, H.; Quidant, R.; Oron, D.; Wenger, J. Excitation enhancement of a quantum dot coupled to a plasmonic antenna. *Adv. Mater.* **2012**, *24*, OP314−OP320.

(20) Akselrod, G. M.; Argyropoulos, C.; Hoang, T. B.; Ciraci, C.; Fang, C.; Huang, J.; Smith, D. R.; Mikkelsen, M. H. Probing the mechanisms of large Purcell enhancement in plasmonic nanoantennas. *Nat. Photonics* **2014**, *8*, 835−840.

(21) Zhou, X.; Deeb, C.; Kostcheev, S.; Wiederrecht, G. P.; Adam, P. M.; Béal, J.; Plain, J.; Gosztola, D. J.; Grand, J.; Félidj, N.; Wang, H.; Vial, A.; Bachelot, R. Selective Functionalization of the Nanogap of a Plasmonic Dimer. *ACS Photonics* **2015**, *2*, 121−129.

(22) Kinkhabwala, A.; Yu, Z. F.; Fan, S. H.; Avlasevich, Y.; Mullen, K.; Moerner, W. E. Large single-molecule fluorescence enhancements produced by a bowtie nanoantenna. *Nat. Photonics* **2009**, *3*, 654−657.

(23) Punj, D.; Mivelle, M.; Moparthi, S. B.; van Zanten, T. S.; Rigneault, H.; van Hulst, N. F.; García-Parajó, M. F.; Wenger, J. A plasmonic antenna-in-box platform for enhanced single-molecule analysis at micromolar concentrations. *Nat. Nanotechnol.* **2013**, *8*, 512−516.

(24) Huang, J. S.; Callegari, V.; Geisler, P.; Brüning, C.; Kern, J.; Prangsma, J. C.; Weinmann, P.; Kamp, M.; Forchel, A.; Biagioni, P.; Sennhauser, U.; Hecht, B. Atomically flat single-crystalline gold nanostructures for plasmonic nanocircuitry. *Nat. Commun.* **2010**, *1*, 150.

(25) Grzelczak, M.; Vermant, J.; Furst, E. M.; Liz-Marzán, L. M. Directed self-assembly of nanoparticles. *ACS Nano* **2010**, *4*, 3591−3605.

(26) Edel, J. B.; Kornyshev, A. A.; Urbakh, M. Self-assembly of nanoparticle arrays for use as mirrors, sensors, and antennas. *ACS Nano* **2013**, *7*, 9526−9532.

(27) Fan, J. A.; He, Y.; Bao, K.; Wu, C.; Bao, J.; Schade, N. B.; Manoharan, V. N.; Shvets, G.; Nordlander, P.; Liu, D.; Capasso, F. DNA-enabled self-assembly of plasmonic nanoclusters. *Nano Lett.* **2011**, *11*, 4859−4864.

(28) Busson, M. P.; Rolly, B.; Stout, B.; Bonod, N.; Larquet, E.; Polman, A.; Bidault, S. Optical and topological characterization of gold nanoparticle dimers linked by a single DNA double strand. *Nano Lett.* **2011**, *11*, 5060−5065.

(29) Busson, M. P.; Rolly, B.; Stout, B.; Bonod, N.; Bidault, S. Accelerated single photon emission from dye molecule-driven nanoantennas assembled on DNA. *Nat. Commun.* **2012**, *3*, 962.

(30) Busson, M. P.; Rolly, B.; Stout, B.; Bonod, N.; Wenger, J.; Bidault, S. Photonic engineering of hybrid metal-organic chromophores. *Angew. Chem., Int. Ed.* **2012**, *51*, 11083−11087.

(31) Acuna, G. P.; Möller, F. M.; Holzmeister, P.; Beater, S.; Lalkens, B.; Tinnefeld, P. Fluorescence enhancement at docking sites of DNA-directed self-assembled nanoantennas. *Science* **2012**, *338*, 506−510.

(32) Thacker, V. V.; Herrmann, L. O.; Sigle, D. O.; Zhang, T.; Liedl, T.; Baumberg, J. J.; Keyser, U. F. DNA origami based assembly of gold nanoparticle dimers for surface-enhanced Raman scattering. *Nat. Commun.* **2014**, *5*, 3448.

(33) Kühler, P.; Roller, E. M.; Schreiber, R.; Liedl, T.; Lohmüller, T.; Feldmann, J. Plasmonic DNA-origami nanoantennas for surface-enhanced Raman spectroscopy. *Nano Lett.* **2014**, *14*, 2914−2919.

(34) Zhang, T.; Gao, N.; Li, S.; Lang, M. J.; Xu, Q. H. Single-Particle Spectroscopic Study on Fluorescence Enhancement by Plasmon Coupled Gold Nanorod Dimers Assembled on DNA Origami. *J. Phys. Chem. Lett.* **2015**, *6*, 2043−2049.

(35) Fan, J. A.; Wu, C.; Bao, K.; Bao, J.; Bardhan, R.; Halas, N. J.; Manoharan, V. N.; Nordlander, P.; Shvets, G.; Capasso, F. Self-assembled plasmonic nanoparticle clusters. *Science* **2010**, *328*, 1135−1138.

DOI: 10.1021/acsphotonics.5b00152
ACS Photonics 2015, 2, 1099−1107

(36) Fan, J. A.; Bao, K.; Sun, L.; Bao, J.; Manoharan, V. N.; Nordlander, P.; Capasso, F. Plasmonic mode engineering with templated self-assembled nanoclusters. *Nano Lett.* **2012**, *12*, 5318−5324.
(37) Kern, J.; Großmann, S.; Tarakina, N. V.; Häckel, T.; Emmerling, M.; Kamp, M.; Huang, J. S.; Biagioni, P.; Prangsma, J. C.; Hecht, B. Atomic-scale confinement of resonant optical fields. *Nano Lett.* **2012**, *12*, 5504−5509.
(38) Cha, H.; Yoon, J. H.; Yoon, S. Probing quantum plasmon coupling using gold nanoparticle dimers with tunable interparticle distances down to the subnanometer range. *ACS Nano* **2014**, *8*, 8554−8563.
(39) Stranahan, S. M.; Titus, E. J.; Willets, K. A. SERS Orientational Imaging of Silver Nanoparticle Dimers. *J. Phys. Chem. Lett.* **2011**, *2*, 2711−2715.
(40) Stranahan, S. M.; Titus, E. J.; Willets, K. A. Discriminating Nanoparticle Dimers from Higher Order Aggregates through Wavelength-Dependent SERS Orientational Imaging. *ACS Nano* **2012**, *6*, 1806−1813.
(41) Estrada, L. C.; Aramendia, P. F.; Martinez, O. E. 10000 times volume reduction for fluorescence correlation spectroscopy using nano-antennas. *Opt. Express* **2008**, *16*, 20597−20602.
(42) Wang, Q.; Lu, G.; Hou, L.; Zhang, T.; Luo, C.; Yang, H.; Barbillon, G.; Lei, F. E.; Marquette, C. A.; Perriat, P.; Tillement, O.; Roux, S.; Ouyang, Q.; Gong, Q. Fluorescence correlation spectroscopy near individual gold nanoparticle. *Chem. Phys. Lett.* **2011**, *503*, 256−261.
(43) Lu, G. W.; Liu, J.; Zhang, T. Y.; Li, W. Q.; Hou, L.; Luo, C. X.; Lei, F.; Manfait, M.; Gong, Q. H. Plasmonic near-field in the vicinity of a single gold nanoparticle investigated with fluorescence correlation spectroscopy. *Nanoscale* **2012**, *4*, 3359−3364.
(44) Dutta Choudhury, S.; Ray, K.; Lakowicz, J. R. Silver nanostructures for fluorescence correlation spectroscopy: reduced volumes and increased signal intensities. *J. Phys. Chem. Lett.* **2012**, *3*, 2915−2919.
(45) Punj, D.; de Torres, J.; Rigneault, H.; Wenger, J. Gold nanoparticles for enhanced single molecule fluorescence analysis at micromolar concentration. *Opt. Express* **2013**, *21*, 27338−27343.
(46) Yuan, H.; Khatua, S.; Zijlstra, P.; Yorulmaz, M.; Orrit, M. Thousand-fold enhancement of single-molecule fluorescence near a single gold nanorod. *Angew. Chem.* **2013**, *125*, 1255−1259.
(47) Khatua, S.; Paulo, P. M.; Yuan, H.; Gupta, A.; Zijlstra, P.; Orrit, M. Resonant plasmonic enhancement of single-molecule fluorescence by individual gold nanorods. *ACS Nano* **2014**, *8*, 4440−4449.
(48) Khatua, S.; Yuan, H.; Orrit, M. Enhanced-fluorescence correlation spectroscopy at micro-molar dye concentration around a single gold nanorod. *Phys. Chem. Chem. Phys.* **2015**, DOI: 10.1039/C4CP03057E.
(49) Langguth, L.; Koenderink, F. A. Simple model for plasmon enhanced fluorescence correlation spectroscopy. *Opt. Express* **2014**, *22*, 15397−15409.
(50) Kinkhabwala, A. A.; Yu, Z. F.; Fan, S. H.; Moerner, W. E. Fluorescence correlation spectroscopy at high concentrations using gold bowtie nanoantennas. *Chem. Phys.* **2012**, *406*, 3−8.
(51) Aouani, H.; Mahboub, O.; Bonod, N.; Devaux, E.; Popov, E.; Rigneault, H.; Ebbesen, T. W.; Wenger, J. Bright unidirectional fluorescence emission of molecules in a nanoaperture with plasmonic corrugations. *Nano Lett.* **2011**, *11*, 637−644.
(52) Mertens, H.; Koenderink, A. F.; Polman, A. Plasmon-enhanced luminescence near noble-metal nanospheres: comparison of exact theory and an improved Gersten and Nitzan model. *Phys. Rev. B: Condens. Matter Mater. Phys.* **2007**, *76*, 115123.
(53) Bharadwaj, P.; Anger, P.; Novotny, L. Nanoplasmonic enhancement of single-molecule fluorescence. *Nanotechnology* **2007**, *18*, 044017.
(54) Stout, B.; Devilez, A.; Rolly, B.; Bonod, N. Multipole methods for nanoantennas design: applications to Yagi-Uda configurations. *J. Opt. Soc. Am. B* **2011**, *28*, 1213−1223.
(55) Stout, B.; Auger, J. C.; Devilez, A. Recursive T matrix algorithm for resonant multiple scattering: applications to localized plasmon excitations. *J. Opt. Soc. Am. A* **2008**, *25*, 2549−2557.
(56) Palik, E.; Ghosh, G. *Handbook of Optical Constants of Solids*; Academic Press: Boston, 1998.

DOI: 10.1021/acsphotonics.5b00152
ACS Photonics 2015, 2, 1099−1107